Smoke-Driven Changes in Photosynthetically Active Radiation During the U.S. Agricultural Growing Season

Kimberley A. Corwin[1], Chelsea A. Corr[2], Jesse Burkhardt[3], and Emily V. Fischer[1]

[1]Department of Atmospheric Science, Colorado State University, Fort Collins, CO. [2]Department of Biology/Chemistry, Springfield College, Springfield, MA. [3]Department of Agricultural and Resource Economics, Colorado State University, Fort Collins, CO.

Corresponding author: Kimberley A. Corwin (kimberley.corwin@colostate.edu)

Key Points:

- Smoke is most prevalent in the atmospheric column over the United States in the mid- to late growing season months of July and August.
- Smoke increases the average diffuse fraction of surface-level photosynthetically active radiation, especially under cloud-free conditions.
- Ground and satellite observations show that diffuse fraction increases and total irradiance decreases with increasing smoke plume thickness.

Abstract

Wildfire smoke frequently blankets the U.S. throughout the agricultural growing season, and this will likely increase with climate change. Studies of smoke impacts have largely focused on air quality and human health; however, understanding smoke's impact on photosynthetically active radiation (PAR) is essential for predicting how smoke affects plant growth. We compare surface shortwave irradiance and diffuse fraction (DF) on smoke-impacted and smoke-free days from 2006-2020 using data from multifilter rotating shadowband radiometers at ten U.S. Department of Agriculture (USDA) UV-B Monitoring and Research Program stations and smoke plume locations from operational satellite products. On average, 20% of growing season days are smoke-impacted, but smoke prevalence increases over time ($r = 0.60$, $p < 0.05$). Smoke presence peaks in the mid- to late growing season (i.e., July, August), particularly over the northern Rocky Mountains, Great Plains, and Midwest. We find an increase in the distribution of PAR DF on smoke-impacted days, with larger increases at lower cloud fractions. On clear-sky days, daily average PAR DF increases by 10 percentage points when smoke is present. Spectral analysis of clear-sky days shows smoke increases DF (average: +45%) and decreases total irradiance (average: -6%) across all six wavelengths measured from 368-870 nm. Optical depth measurements from ground and satellite observations both indicate that spectral DF increases and total spectral irradiance decreases with increasing smoke plume optical depth (i.e., plume thickness). Our analysis provides a foundation for understanding smoke's impact on PAR, which carries implications for agricultural crop productivity under a changing climate.

Plain Language Summary

Wildfires in the United States (U.S.) are occurring more often and burning larger areas, and smoke from these fires impacts incoming solar radiation across the country. Sunlight is a necessary ingredient for photosynthesis with the total amount and diffuse fraction of light affecting plant growth. Smoke particles absorb and scatter light resulting in less total and more diffuse radiation, respectively. Since smoke is present over agricultural regions during the growing season (April-September), understanding how smoke affects sunlight is essential for determining smoke's impact on crops. We use ground-based measurements of solar radiation and satellite-based observations of smoke plume location and thickness to examine how sunlight varies on days with and without smoke at ten agriculturally-important locations across the U.S. from 2006-2020. We show that smoke is present most often during the mid- to late growing season when light characteristics most impact plant growth. One in five growing season days is smoke-impacted and smoke is becoming more frequent over time. The diffuse fraction is higher on smoke-impacted days with the largest increase occurring when cloud cover is low. While the diffuse fraction increases with smoke, total irradiance decreases, and these shifts grow stronger as smoke plumes become thicker.

1 Introduction

Since the mid-1980s, higher spring and summer temperatures, earlier snowmelt, and increased fuel aridity have led to longer wildfire seasons with fires that burn longer and cover larger areas (Abatzoglou & Williams, 2016; Westerling, 2016; Westerling et al., 2006). Much of the increase in U.S. wildfire activity has been centered in the Pacific Northwest and Southwest (Westerling, 2016). The increase in wildfire activity is increasing wildfire smoke emissions (Ford et al., 2018; Yue et al., 2013). Existing smoke climatologies show that wildfire smoke from the western U.S. travels far from active fire sources to affect the atmospheric column and air quality nationally (Brey et al., 2018; O'Dell et al., 2021). However, the widespread reach of wildfire smoke was documented prior to the severe western U.S. wildfire seasons of 2018, 2020, and 2021 (Brey et al., 2018), which may be emblematic of future wildfire conditions (Abatzoglou et al., 2021; Higuera & Abatzoglou, 2021).

Increases in wildfire activity are causing measurable changes in atmospheric properties over the U.S. (e.g., Buchholz et al., 2022; Xue et al., 2021). For example, near the surface, fine particulate matter ($PM_{2.5}$) attributable to anthropogenic sources is declining over the U.S. due to regulations that have substantially reduced anthropogenic emissions over the last two decades. At the same time, studies of surface $PM_{2.5}$ concentrations show that wildfire smoke emissions are offsetting the reductions in $PM_{2.5}$ caused by declining anthropogenic emissions, particularly in the Pacific Northwest (McClure & Jaffe, 2018; O'Dell et al., 2019). Climate-driven wildfire emissions are projected to become the dominant source of summertime $PM_{2.5}$ in the western U.S. during the 21st century (Ford et al., 2018; Val Martin et al., 2015).

Recent trends in surface $PM_{2.5}$ are similar to aerosol optical depth (AOD) trends (e.g., Hallar et al., 2017; McClure & Jaffe, 2018), which account for aerosols throughout the atmospheric column. Aerosols throughout the atmospheric column change the amount and characteristics of shortwave irradiance reaching the Earth's surface. Direct interactions between aerosols and radiation stem from aerosol absorption and scattering of downwelling shortwave solar radiation. Absorption decreases total downwelling solar irradiance while scattering changes the ratio of direct-to-diffuse irradiance by increasing the diffuse fraction (DF). There are also indirect aerosol effects from aerosol-cloud interactions. Ultimately, by changing surface shortwave radiation levels, aerosols, including those from wildfires, can influence Earth systems that rely on radiation to function, such as plant productivity.

Photosynthetically active radiation (PAR) refers to solar radiation at wavelengths from 400-700 nm, which plants use for photosynthesis. Direct radiation benefits sunlit leaves, while diffuse radiation is able to reach shaded leaves and boost productivity, particularly when sunlit leaves reach saturation. Reducing total PAR via aerosol absorption can negatively impact plant productivity, but increasing the DF via aerosol scattering can result in more efficient use of available light, a phenomenon known as the diffuse radiation fertilization effect (DRFE; Greenwald et al., 2006; Kanniah et al., 2012; Knohl & Baldocchi, 2008; Schiferl & Heald, 2018). The degree to which the DRFE benefits productivity depends the tradeoff between decreasing total PAR and increasing PAR DF as well as on plant traits such as canopy structure, leaf area index, and photosynthetic pathway (e.g., C_3 or C_4), which determine the extent of shaded leaves and light saturation (Kanniah et al., 2012). Few studies examine wildfire smoke's impact on the DRFE, but the existing literature indicates that understanding how smoke affects surface radiation may be important for productivity (Hemes et al., 2020; Lee et al., 2022; McKendry et al., 2019). Therefore, large-scale longitudinal studies of smoke-radiation interactions that are based on observational data are needed to better understand smoke's impact on ecosystems and, given the prevalence of smoke over agricultural land, on food systems (Brey et al., 2018).

We present an analysis of smoke trends and associated changes to surface-level shortwave radiation at 10 sites across the contiguous U.S. from 2006-2020. We leverage observational data from ground-based in-situ radiation measurements and satellite observations of wildfire smoke, clouds, and AOD to examine 1) how wildfire smoke varies spatially and temporally during the growing season across the U.S. and 2) how total PAR and PAR DF at the surface vary with wildfire smoke. We focus our analysis on the main agricultural growing season (April-September) in the U.S. and over agriculturally-important regions.

2 Methods

This analysis leverages radiation, smoke plume, cloud, and aerosol datasets from ground and satellite observations. Detailed descriptions of each dataset are presented in the following sections. Data processing and analysis are summarized in Figure 1.

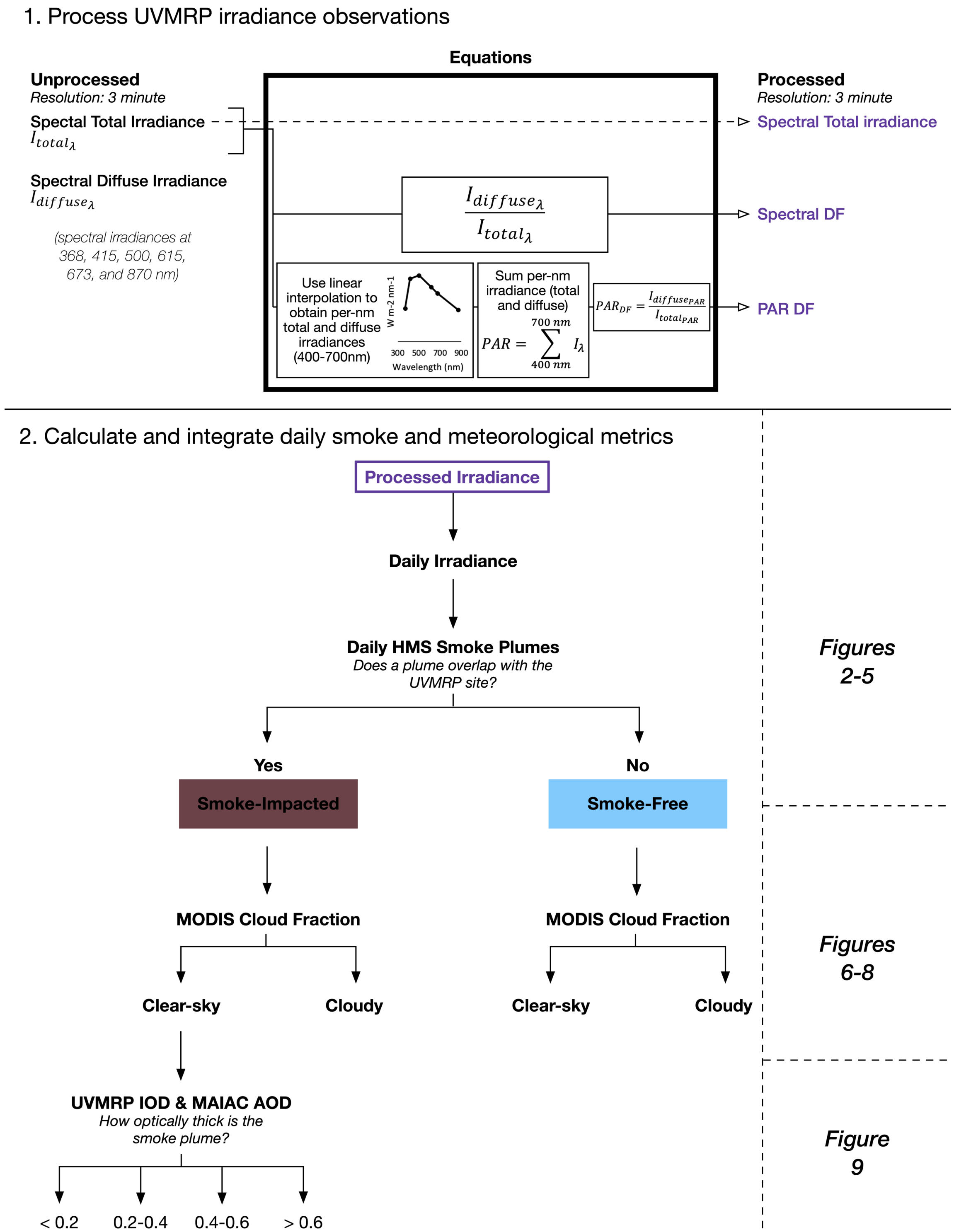

Figure 1: Diagram summarizing data processing and integration for the irradiance (UVMRP), smoke plume (HMS), cloud (MODIS), and optical depth (UVMRP & MAIAC) datasets used for this analysis.

2.1 UVMRP Shortwave Radiation Data

The United States Department of Agriculture's (USDA) UV-B Monitoring and Research Program (UVMRP; https://uvb.nrel.colostate.edu/UVB; Bigelow et al., 1998) observes surface-level solar radiation using a network of 38 active sites across the U.S., Canada, South Korea, and New Zealand. Most monitoring sites (34) are distributed across the continental U.S. in agriculturally-important regions as the program's primary goal is to develop a UV-B climatology to better understand how UV-B radiation impacts agricultural crop and animal production (Bigelow et al., 1998). We focus on data from 10 UVMRP sites (Table 1) selected for their proximity to agricultural areas and, with the exception of the California site, their distance from major metropolitan areas that contribute to aerosol loading. The sites are distributed across eight of the U.S. regions analyzed in the Brey et al. (2018) smoke climatology, which are largely similar to the EPA regions, allowing broad spatial coverage. We refer to these sites by their geographical region code listed in Table 1.

Table 1

Description of UVMRP Site Locations and Data Availability

Site	Location	Region[a]	Smoke indicator[b]	Irradiance (Total & DF)[c]	IOD[c]	AOD[d]	CF[e]	Overall	Smoke-free days	Smoke-impacted days
Davis, California	38.53 N, 121.78 W	Southwest (SW)	99%	98%	92%	89%	100%	80%	1868	334
Pullman, Washington	46.76 N, 117.19 W	Northwest (NW)	99%	95%	78%	70%	100%	53%	1050	398
Poplar, Montana	48.31 N, 105.10 W	Rocky Mountain (RM)	99%	94%	98%	66%	100%	62%	1156	541
Pawnee, Colorado	40.81 N, 104.76 W	Rocky Mountain (RM)	99%	78%	75%	70%	100%	51%	1176	232
Fargo, North Dakota	46.90 N, 96.81 W	Great Plains (GP)	99%	94%	92%	59%	100%	51%	843	570
Billings, Oklahoma	36.60 N, 97.49 W	Southern Plains (SP)	99%	89%	82%	67%	100%	53%	1099	356
Grand Rapids, Minnesota	47.18 N, 93.53 W	Midwest (MW)	99%	95%	97%	51%	100%	48%	825	500
Bondville, Illinois	40.05 N, 88.37 W	Midwest (MW)	99%	83%	84%	53%	100%	43%	836	335
Starkville, Mississippi	33.47 N, 88.78 W	Southeast (SE)	99%	84%	79%	61%	100%	45%	1095	133
Geneva, New York	42.88 N, 77.03 W	Northeast (NE)	99%	91%	97%	53%	100%	48%	1125	201

Note: Analyses that contain a subset of the data products listed used the maximum number of data points available. At each site, 100% coverage of 15 growing seasons equals 2,745 days. [a]Regions from Brey et al. (2018). [b]HMS smoke product. [c]UVMRP irradiance and instantaneous cloud-aerosol optical depth product. [d]MAIAC aerosol optical depth product. [e]MODIS cloud fraction product.

Each UVMRP station is equipped with two multifilter rotating shadow-band radiometers (MFRSR) that measure total horizontal and diffuse-horizontal solar irradiance at seven wavelength passbands with a three-minute temporal resolution. The ultraviolet instrument (UV-MFRSR) measures irradiance at 300, 305, 311, 317, 325, 332, and 368 nm with a full-width at half maximum (FWHM) of 2 nm. The visible instrument (VIS-MFRSR) measures irradiance at 415, 500, 615, 673, 870, and 940 nm with a FWHM of 10 nm. The simultaneous collection of total and diffuse irradiance by the same MFRSR instrument allows for the real-time calculation of spectrally-resolved direct normal irradiance which supports continued calibration via Langley analysis (Harrison et al., 1994) and the determination of total optical depth and instantaneous cloud-aerosol combined optical depth at the same temporal resolution. Langley calibration eliminates concerns that independent sensor drift could bias diffuse fraction calculations. Drift may impact total PAR calculations, but all UVMRP sites maintain broadband PAR pyranometers for independent validation of total PAR. Calibration and validation details are available in Bigelow et al. (1998). As an operational program, the UVMRP provides routine maintenance and calibration of sensors to ensure reliable and relatively consistent data products for public use; however, the instrument fleet is aging as coverage spans nearly three decades at some sites.

We examined fifteen years (2006-2020) of irradiance records for the 10 sites in Table 1. We limited our study to the six UV- and VIS-MFRSR bands that provide full coverage of the PAR wavelength range: 368, 415, 500, 615, 673, and 870 nm. We performed multiple data cleaning and quality control operations that are described in detail below. From the remaining three-minute UVMPR records, we calculated daily average values for the following variables: total spectral irradiance, spectral DF, total PAR irradiance, PAR DF, and instantaneous cloud-aerosol combined optical depth (IOD). All analyses were performed using daily average values for integration with satellite smoke, aerosol, and cloud products. An outline of the data processing and integration steps with associated figures is provided in Figure 1.

For data cleaning and quality control, we removed missing data and records with quality control flags that indicated whole instrument or individual channel damage or degradation. We only considered records for which irradiance data were available across all six wavelengths of interest. Occasional gaps exist due to instrument damage or maintenance. After implementing quality controls, we removed any records where the solar zenith angle was greater than 75 degrees to focus on core daylight hours when plants may reach light saturation and experience benefits from the DRFE. We removed all records containing negative irradiance values in the total, direct, and diffuse component and any time periods in which all spectrally-resolved total irradiance values equal zero.

Data anomalies were present across multiple sites and years, characterized by irradiance values that far exceeded the peak solar irradiance at the measured wavelengths. These anomalies impacted all bands on either the UV- or VIS-MFRSR but occurred infrequently, affecting only 0.09% of the nearly 8.29 million three-minute cleaned records across all ten sites. To ensure that only physically reasonable values were included in the analysis, we removed records with total irradiances in excess of threshold values. Since the UVMRP site in New Mexico observes some of the highest irradiance values and lowest cloud interference in the network, we used data from the New Mexico UVMRP site to approximate the maximum spectral irradiance possible for use as a network threshold. We removed all records with an irradiance greater than 110% of the maximum spectrally-resolved irradiance recorded in New Mexico from 2006-2020. As such, we remove records that exceed the following thresholds: 1.26 W/m^2 for 368 nm, 2.42 W/m^2 for 415 nm, 2.53 W/m^2 for 500 nm, 2.42 W/m^2 for 615 nm, 2.27 W/m^2 for 673 nm, and 1.37 W/m^2 for 870 nm. Overall, the volume of data available helps reduce the impact of anomalies removed during the data cleaning process.

Ultimately, we are interested in understanding how the overall diffuse fraction of PAR varies, which requires estimating the total and diffuse irradiance over the entire 400-700 nm range. We performed a linear interpolation between six adjacent wavelength bands spanning 368-870 nm to estimate the per-nanometer irradiance from 400-700 nm for both total and diffuse irradiance (Figure 1). While the solar spectrum is not linear, we can approximate the overall shape of the spectral curve using these six closely-spaced MFRSR bands, especially since the 500 nm channel nearly captures the peak wavelength of solar irradiance. We summed the interpolated values to obtain total and diffuse PAR. A comparison of the interpolated total PAR values to total PAR measured by a collocated broadband PAR LI-190SA Quantum Sensor from LI-COR for a subset of years (2015-2019) at the Pawnee, CO site is included in the SI (Figure S1). All calculated PAR and retrieved spectral values were then averaged to the daily level, and the resulting site specific data availability ranged from 78% to 98% (Table 1).

2.2 HMS Smoke Plume Data

The Hazard Mapping System (HMS; https://www.ospo.noaa.gov/Products/land/hms.html) operated by the National Oceanic and Atmospheric Administration's (NOAA) National Environmental Satellite, Data, and Information Service (NESDIS) uses data from polar orbiting and geostationary satellites to provide daily operational smoke plume extents across North America in near real-time. The HMS became operational in 2003 for the U.S. and Canada, expanding to full North American coverage with the incorporation of Mexico and Central America in 2006 (Ruminski et al., 2006). Spatial coverage of the HMS spans from 14.6°N to 72°N and 50°W to 170°W and captures each region's primary biomass burning season. Smoke plumes are identified and outlined manually by analysts using 2-km or finer resolution visual-band imagery from the GOES satellites. Analysts rely on a series of images taken throughout the day, but primarily those near sunset and sunrise when smoke plumes are most visible. Occasionally, analysts reference observations from polar-orbiting satellites to identify smoke as well as use infrared bands to distinguish between clouds and smoke (Rolph et al., 2009).

Multiple limitations characterize the HMS smoke plume data and impact potential uses of the data. Because the smoke product relies on visible imagery, no information about smoke plume location or extent is available at night. Analysts make no attempt to identify the smoke's source. As such, smoke plumes may originate from wildfires, agricultural burning, or prescribed burning. The HMS also struggles to distinguish between smoke and anthropogenic haze when smoke becomes lofted, travels far from its source, and mixes with pollutants. The difference between clouds and smoke is similarly difficult to discern from visual imagery, and although infrared channels can help, untangling when clouds obscure smoke is a challenge. Overall, the greatest area of uncertainty exists at the edge of the plume, where determining the extent of thin smoke is difficult. Areas with high albedos, such as snow, also pose a challenge for identifying smoke particles. These limitations make the HMS smoke product a conservative estimate of smoke plume number and extent (Brey et al., 2018).

We use the HMS smoke product to distinguish between smoke-free and smoke-impacted days at each UVMRP station. We use the HMS shapefiles, extract the smoke plume polygons, and determine if a polygon overlaps with a UVMRP station. Site-specific results for growing season days are merged with the associated daily average radiation metrics for analysis (Figure 1). HMS data coverage is 99% at all UVMRP sites as missing data between April 1 and September 30 for 2006-2020 impact all sites equally.

2.3 MODIS Cloud Fraction Data

The Moderate Resolution Imaging Spectroradiometer (MODIS) instrument provides daily satellite imagery from the National Aeronautics and Space Administration (NASA) Earth Observing System's (EOS) Terra and Aqua satellites. The MODIS level-3 gridded atmosphere daily global joint product (Platnick et al., 2015) provides average cloud fraction (CF) at a spatial resolution of 1 x 1 degree. Terra and Aqua overpasses capture morning (~10:30 AM local time) and afternoon (~1:30 PM local time) conditions, respectively.We use both the Terra (MOD08_D3) and Aqua (MYD08_D3) products to calculate an average daytime CF for all days over each site. Since we are interested in daylight hours when the solar zenith angle is smallest and plant light saturation is most likely to occur, the absence of observations in the early morning and late afternoon when the solar zenith angle is large is expected to be less important for applications of the current work. Additionally, the resolution of MODIS products captures the region surrounding UVMRP sites but may not represent the exact conditions observed by the MFRSR. For example, irradiance and optical depth measurements can be heavily influenced by an optically thick but isolated cloud over the site while the satellite-observed CF will remain low. The temporal resolution helps mitigate the impact of rapidly changing cloud cover on daily average irradiance and optical depth measurements. Finally, using MODIS to determine cloud cover under smoke-impacted conditions poses a challenge because MODIS algorithms struggle to distinguish clouds from smoke, leading to the misclassification of thick smoke as cloud cover. However, smoke-impacted days with high CFs (> 0.8) make up only 3.4% of all days across the ten UVMRP sites selected and 1.1% of days that also have UVMRP radiation data available. As such, we expect that cloud-smoke confusion is a minor issue at most sites we examine. We note where cloud-smoke misclassification may impact our analyses below.

2.4 MAIAC Aerosol Optical Depth Data

The Multi-Angle Implementation of Atmospheric Correction (MAIAC; https://modis-land.gsfc.nasa.gov/MAIAC.html) algorithm determines AOD using MODIS data from both the Terra and Aqua satellites. Described in detail by Lyapustin et al. (2018) and Lyapustin and Wang (2018), MAIAC leverages the different spatial and temporal variability of land surfaces and aerosols to improve cloud masking capabilities and retrieve high resolution (1 km) AOD. Land cover can change quickly over short distances but remains relatively stable over short periods of time. In contrast, aerosols are relatively uniformly distributed spatially (i.e., in 1 km x 1 km grids) but can change rapidly over a short period of time. MAIAC uses time series analysis of the land surface reflectance to identify recent clear-sky land cover conditions and detect changes due to clouds or aerosols.

More precisely, MAIAC transforms the 1 km gridded L1B MODIS data into 1200 km^2 tiles corresponding to the MODIS sinusoidal grid. Terra and Aqua overpasses are combined, and the number of orbits recorded for each tile ranges from 1-2 at the equator to up to 16 at higher latitudes. MAIAC uses a sliding window technique to store MODIS imagery from previous days and identify a recent clear-sky reference image for each 1 km grid cell. MAIAC compares the most recent image to the clear-sky reference to construct a cloud mask and then performs a smoke test to reduce the misclassification of thick plumes as clouds and ensure an AOD retrieval. The smoke test compares changes in the deep blue (0.412 um) shortwave band to reflectance at longer red (0.646 um) and blue (0.466 um) wavelengths. Smoke increases attenuation in the 0.412 um band because of greater multiple scattering by aerosols and stronger shortwave absorption by organic carbon. If smoke is detected, MAIAC retrieves an AOD even if the cloud mask indicates a possibly cloudy pixel. Otherwise, MAIAC AOD is only retrieved for clear-sky conditions. The improved cloud detection and screening with MAIAC allows for more accurate AOD computations. MAIAC has been shown to correspond well with AERONET measurements (Lyapustin et al., 2018) and outperform the Dark Target and Deep Blue AOD retrieval algorithms on multiple metrics (Jethva et al., 2019).

We use the 550 nm AOD retrievals available in the daily atmosphere MAIAC product (MCD19A2) to calculate an average daily AOD for all growing season days from 2006-2020. We include data from both the morning (Terra) and afternoon (Aqua) orbits in our calculations to better characterize the overall daytime average AOD. After identifying which MODIS tile contains each of the 10 UVMRP sites in Table 1, we identify the 1 km grid cell (pixel) containing the site location. We extract the overlapping pixel and the 16 nearest neighbors to create a 5 x 5 km box around each site. Given our focus on smoke plumes, which often exhibit high spatial variability, we include possibly cloudy skies in our analysis in addition to the clear-sky best quality AOD values. Prior to calculating an average AOD for each site, we remove any AOD surrounded by eight cloudy pixels (i.e., entirely surrounded by clouds) as this value may represent an anomalous detection.

3 Results and Discussion

3.1 Monthly Average Smoke Frequency During the Growing Season

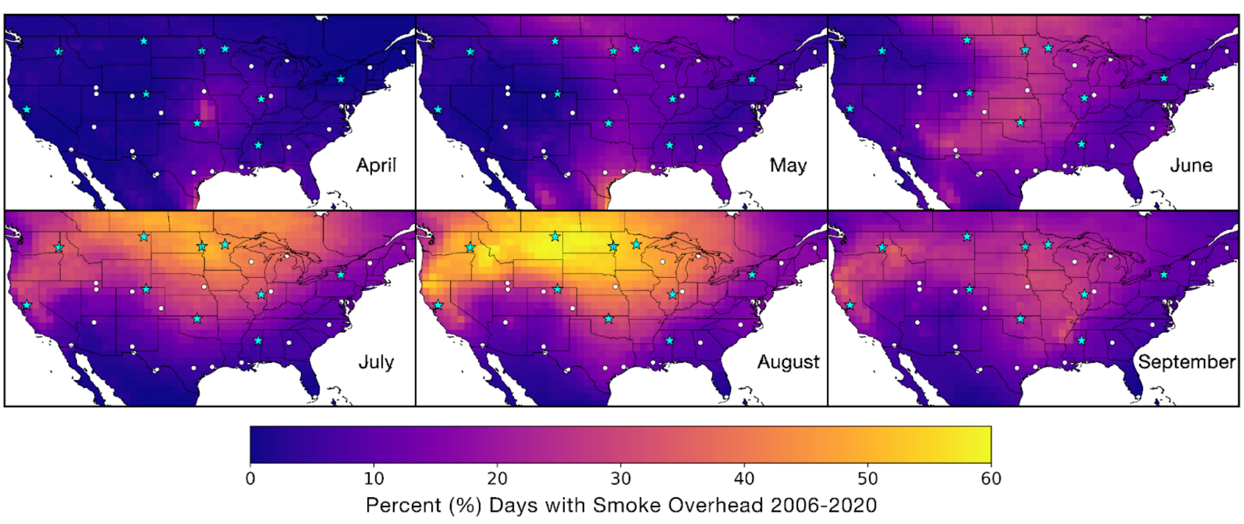

Figure 2: Average percentage of smoke-impacted days per growing season month (April-September) from 2006-2020 based on the overlap of the HMS Smoke Product plume polygons

with the centroid of a 1-degree grid. Blue stars indicate the ten sites analyzed here and the white circles show the remaining UVMRP network sites in the continental U.S.

Smoke frequency and timing varies regionally across the continental U.S. between April and September, the primary agricultural growing season (Figure 2). At the start of the growing season, smoke-impacted days are infrequent but most common in the SP, GP, and western MW. The particularly high frequency of smoke over eastern Kansas in April (~25% of days) coincides with the Flint Hills region. Prescribed fires are used to preserve Flint Hills grasslands in the spring with the bulk of the burning occurring in April (Baker et al., 2019; Möhler & Goodin, 2012). In May, smoke-impacted days remain infrequent and still mainly occur in the SP, GP, and MW. The higher frequency of smoke-impacted days in the SP and GP in the early growing season may result from smoke transported from southern Mexico and Central America where fire starts are common in April and May (Peppler et al., 2000; Rogers & Bowman, 2001; J. Wang et al., 2009; S. C. Wang et al., 2018). In June, an increase in smoke-impacted days is evident over Arizona and New Mexico, which is consistent with earlier fire start times (Westerling et al., 2003) and the predominance of local smoke (Brey et al., 2018) in this region. Fire starts shift north and northwest as the season progresses (Westerling et al., 2003), which results in increasingly frequent locally-sourced smoke over California and the NW and RM regions in July and August. At the same time, almost all areas of the GP and MW, which are major agricultural regions, experience smoke overhead for at least 30% of August days, which is consistent with findings in Brey et al. (2018) that smoke is transported into these regions from the SW, NW, RM, and Canada. Locations in the northern RM and GP regions, including western Montana and North Dakota, experience smoke on nearly 60% of all August days on average. Ultimately, smoke frequency peaks during the mid- to late growing season across most of the U.S. due to large western wildfires. Smoke-impacted days decline in September, persisting mostly over California and the NW where local fires continue to produce smoke (Westerling et al., 2003).

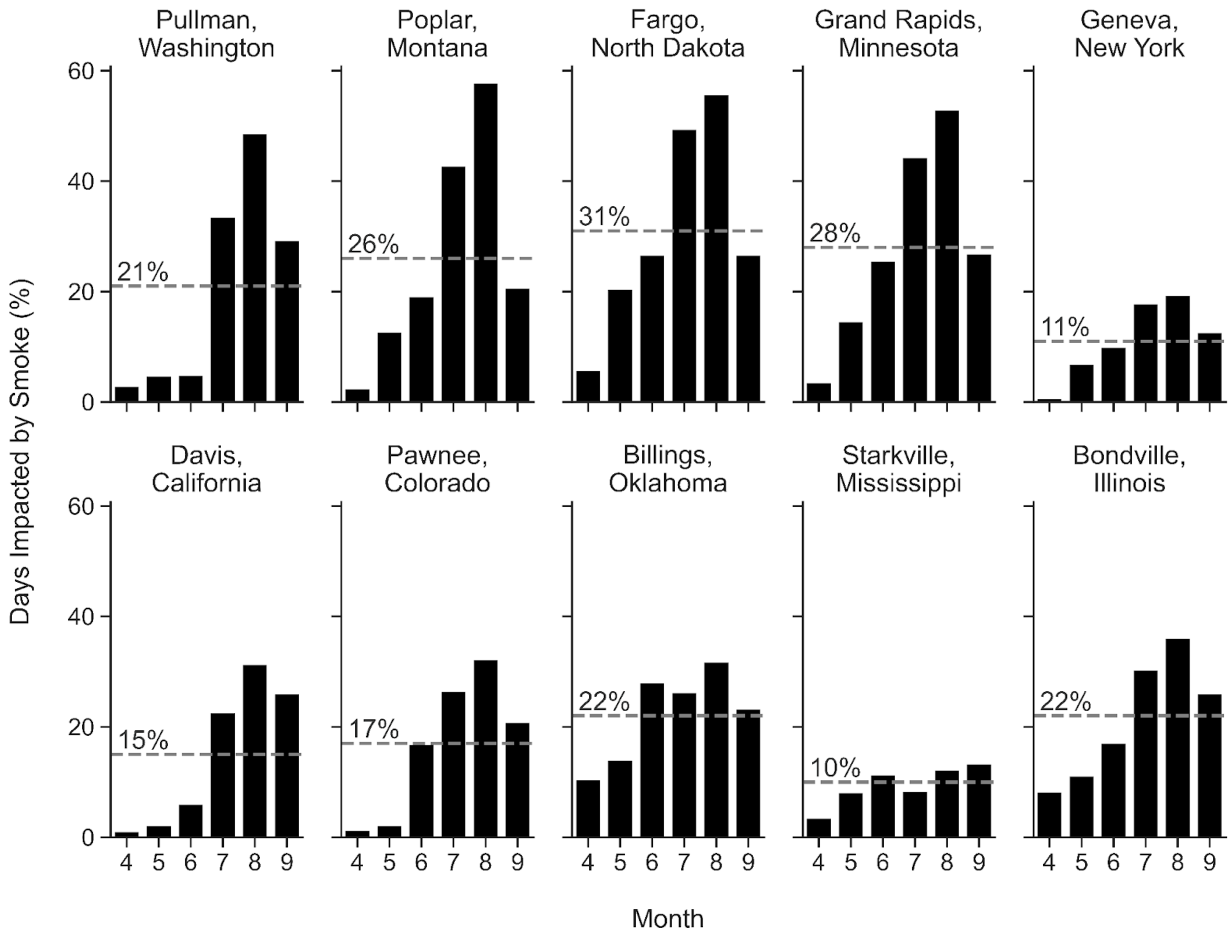

Figure 3: Overall (dashed line) and monthly (black bars) percentage of growing season (April-September) days impacted by smoke at each UVMRP site from 2006-2020. The top row corresponds to more northern sites and the bottom to more southern sights with western sites on the left and eastern sites on the right.

Similar to the HMS trends shown in Figure 2, the 10 UVMRP sites demonstrate distinct differences in monthly smoke frequency across the 15 years of growing seasons analyzed (Figure 3). At all sites, smoke impacts an average of 20% of all growing season days, ranging from 4% in April to 38% in August (Figure S2). Smoke-impacted days are most common in the mid- to late growing season across sites in all regions except the SE. Smoke becomes increasingly more frequent as the growing season progresses with a peak in August at all sites where the smoke primarily stems from wildfires in the western U.S. (i.e., SW, NW, and RM; Brey et al., 2018) and Canada. Northern sites in the RM, GP, and MW regions experience the most smoke-impacted days during the growing season with over a quarter (26-31%) of all days, and over half (53-58%) of all August days, characterized by smoke overhead. Sites in the SW, NW, and southern RM regions experience similar monthly smoke patterns, but the magnitude of smoke frequencies is lower (average: 15-21%). The SW and NW sites tend to experience smoke from local sources compared to the northern RM, GP, and MW regions where smoke from multiple regions is transported overhead, leading to more smoke-impacted days (Brey et al., 2018).

The NE and SE sites experience the least number of smoke-impacted days across the 10 UVMRP locations (Figure 3). The NE site is characterized by temporal smoke patterns similar to those found at other sites, which is consistent with the similar smoke origins documented by Brey et al. (2018). However, the SE site exhibits distinctly different smoke patterns with minimal variability in smoke frequency between May and September. Smoke in the SE region is sourced from a different location than smoke over most other U.S. regions, consistent with this difference. The SE is primarily impacted by local smoke stemming from nearby fires as opposed to the fires in the SW, NW, RM, or Canada (Brey et al., 2018).

3.2 Interannual Variability Of Smoke Overhead During the Growing Season between 2006 and 2020

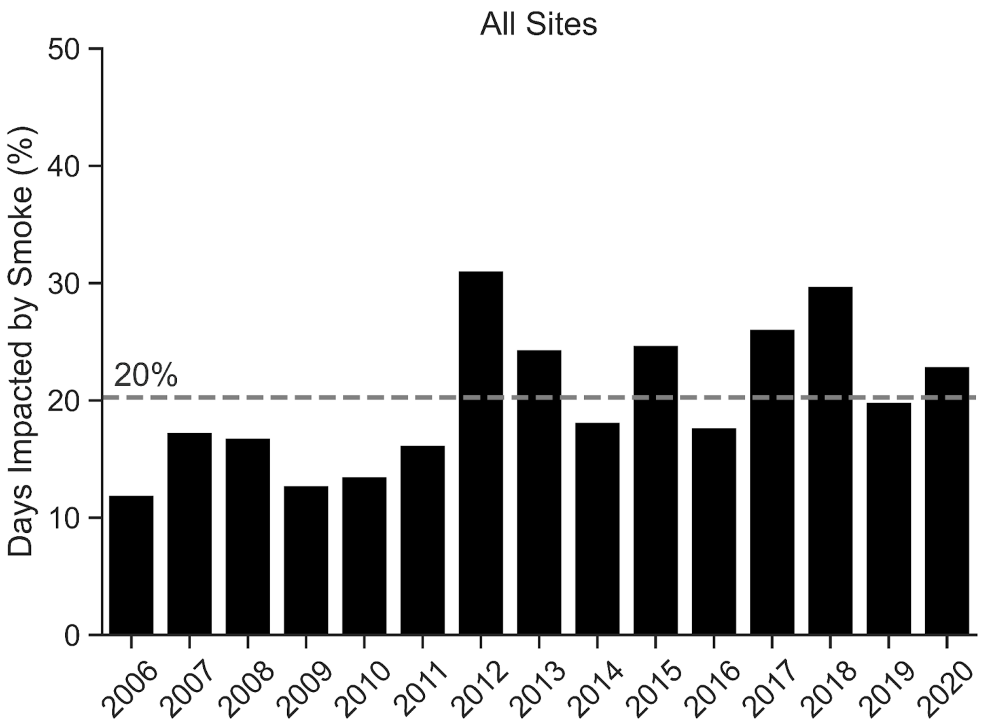

Figure 4: Overall (dashed line) and yearly (black bars) percentage of days during the growing season (April-September) from 2006-2020 with smoke present in the atmospheric column above the 10 UVMRP sites analyzed.

Between 2006 and 2020, the 10 UVMRP sites experienced smoke overhead on 20% of growing season days on average (Figure 4). However, sizable interannual variability in smoke exposure is evident in Figure 4; annual smoke frequencies at the 10 stations range from 12% to 31% of growing season days. Multiple heavy smoke years are included in the record, including 2012 and 2018, which result in 31% and 30% smoke-impacted days, respectively. The percentage of growing season days impacted by smoke increases over time with a positive Pearson's correlation coefficient of 0.60 (p-value < 0.05). Such an increase in smoke frequency is consistent with increasing wildfire frequency, burn area, and season length (Abatzoglou & Williams, 2016; Westerling, 2016; Westerling et al., 2006).

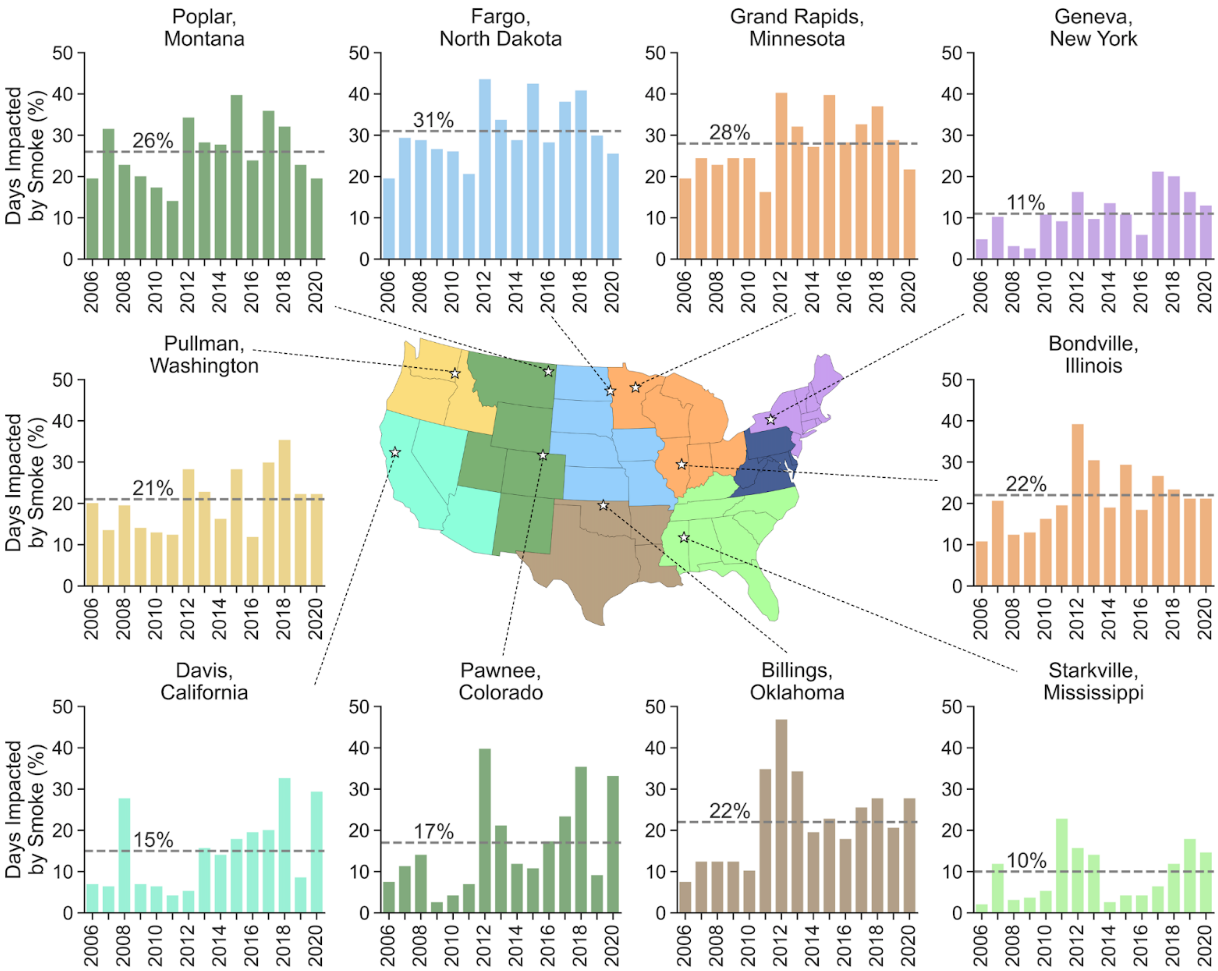

Figure 5: Overall (dashed line) and yearly (region-colored bars) percentage of smoke-impacted days during the growing season (April-September) at each UVMRP site analyzed showing the spatial and temporal variability of wildfire smoke across the U.S. from 2006-2020.

Figure 5 shows that smoke affects all sites during the growing season across all years from 2006-2020. The northern RM, GP, and MW sites are located far downwind of western wildfires but generally experienced higher percentages of smoke-impacted days (26-31%) during the growing season than do sites in the SW, NW, and southern RM (15-21%) that are closer to fires. Northern and Midwestern sites face smoke from multiple western U.S. regions and Canada. Smoke frequency peaks at the SW and southern RM sites during locally severe wildfires seasons. The 2008, 2018, and 2020 wildfire seasons were some of the worst in California state history, and the percentage of smoke-impacted days is 18 percentage points higher in these high smoke years (30%) than the average across all other years (11%). Similarly, Colorado’s severe wildfire seasons in 2012, 2018, and 2020 increased smoke-impacted days by 24 percentage points on average (high smoke average: 36%; low smoke average: 12%). Even within different regions, smoke frequency varies substantially with latitude. In the RM region, the interannual trends differ between the Montana and Colorado sites. The former is more consistently impacted during the growing season while the latter shows distinct peaks in exposure amid overall fewer smoke days. A similar trend is evident in the MW when comparing the Minnesota and Illinois sites.

3.3 Impact of Smoke on PAR Diffuse Fraction Under Variable Cloud Conditions

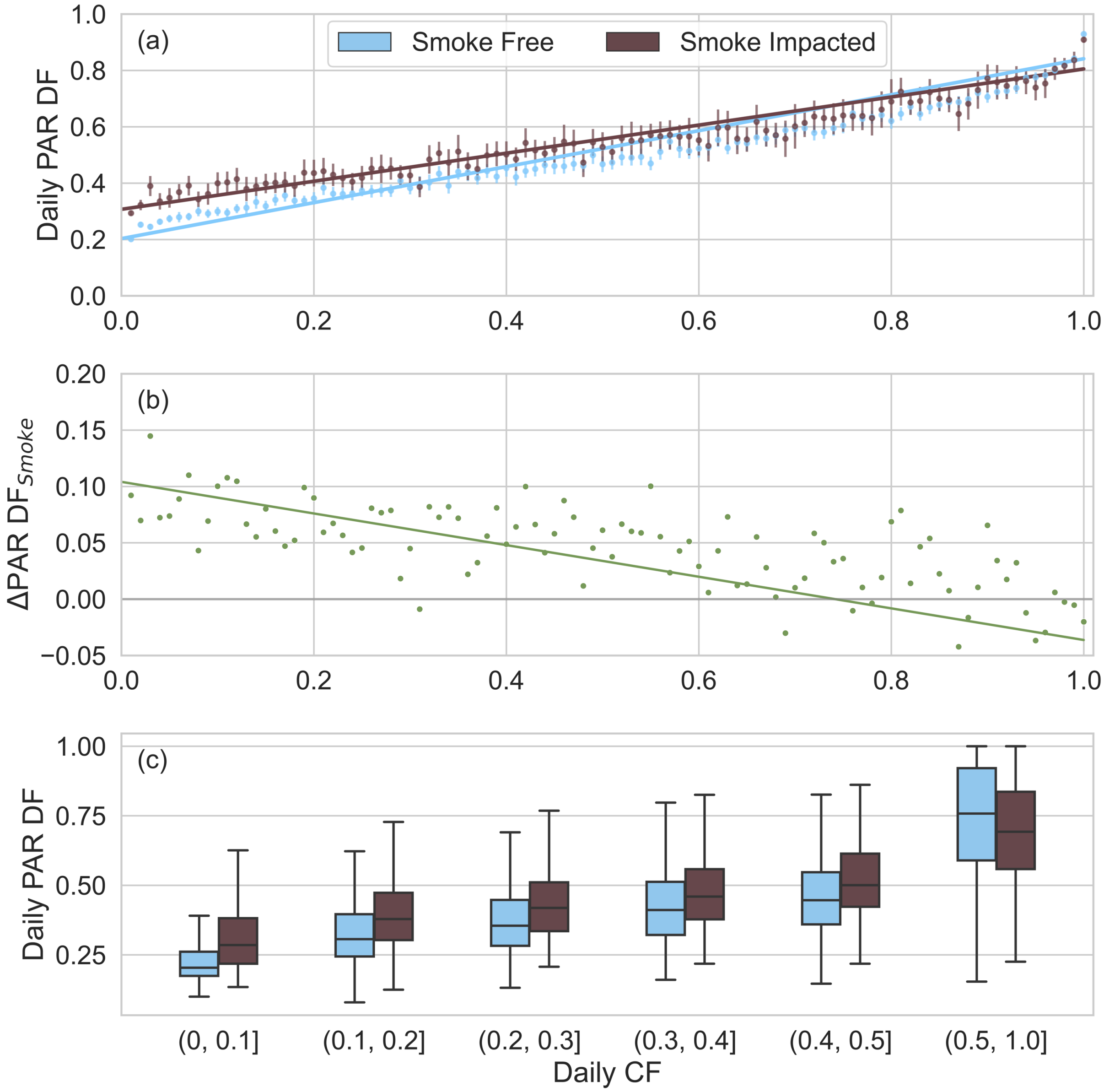

Figure 6: (a) Daily PAR DF based on daily CF on smoke-impacted (brown) and smoke-free (blue) days. Lines show the results of a linear regression analysis using data from all growing season days and all sites from 2006-2020 on smoke-impacted (PAR DF = 0.50CF+0.31, $r = 0.78$, $p < 0.0001$, $n = 4,967$) and smoke-free (PAR DF = 0.64CF+0.20, $r = 0.88$, $p < 0.0001$, $n = 19,486$) days. Data variability is visualized as points representing the average daily PAR DF in each CF bin (interval = 0.01) and vertical lines displaying the 95% confidence intervals for each point. (b) Change in daily PAR DF (ΔPAR DF_{Smoke}) between smoke-impacted and smoke-free days across all CFs. The green line shows the difference between the two linear regression lines in panel a and the green points show the difference between the average daily PAR DF for each CF bin (interval = 0.01). (c) Distribution of daily PAR DF on smoke-impacted (brown) and

smoke-free (blue) days grouped by daily CF at an interval of 0.1 up to a CF of 0.5. The midline refers to the median, and the whiskers indicate the spread of all remaining data excluding outliers. Outliers are defined as PAR DF values falling outside 1.5 times the interquartile range. The bottom and top of the boxes represent the lower and upper quartile, respectively.

Figure 6 compares PAR DF on all study days based on smoke and cloud conditions to approximate the relative importance of the smoke. Linear regression analyses (Figure 6a) show that daily PAR DF increases with increasing CF for both smoke-impacted (DF = 0.50CF+0.31, r = 0.78, $p < 0.0001$) and smoke-free (DF = 0.64CF+0.20, r = 0.88, $p < 0.0001$) days. PAR DF on smoke-impacted days increases the most under clear-sky conditions (+0.10; Figure 6b). This 10 percentage point increase in clear-sky PAR DF results in a PAR DF equivalent to what is experienced on smoke-free days with a CF of 0.16. A PAR DF of 0.45, which Knohl and Baldocchi (2008) determined produced the optimal DRFE, occurs at lower CF values on smoke-impacted (CF = 0.29) than smoke-free (CF = 0.39) days. As cloud cover increases, smoke's relative influence on scattering decreases, resulting in progressively smaller increases in PAR DF on smoke-impacted days. When daily CF reaches 0.75, PAR DF no longer increases with the addition of smoke (Figure 6b).

Figure 6c shows how the distribution of daily PAR DF varies by CF and focuses on days with minimal cloud cover ($CF \leq 0.5$) since Figure 6b shows these days exhibit the largest increase in PAR DF. A clear upward shift in the PAR DF distribution occurs on smoke-impacted days with a CF at or below 0.5. Data from days with $CF > 0.5$ are grouped together and show that smoke fails to increase PAR DF at high CFs. Much of the interquartile range for smoke-impacted days overlaps with that for smoke-free days with the addition of smoke. We expect the impact of smoke on PAR DF to decline with increasing CF as scattering from clouds overwhelms the contribution of smoke scattering to PAR DF. Historically, MODIS CF algorithms have struggled to distinguish between thick smoke plumes and clouds, which results in artificially high CFs under thick smoke conditions. A subset of the smoke-impacted days in the high CF bin should be redistributed across the lower CF bins, thereby adding more thick smoke days with high PAR DF to the lower CF bins. Such a redistribution would increase PAR DF at low CFs, meaning the increase in PAR DF on smoke-impacted days shown in Figure 6 represents a conservative estimate of smoke's radiative effects.

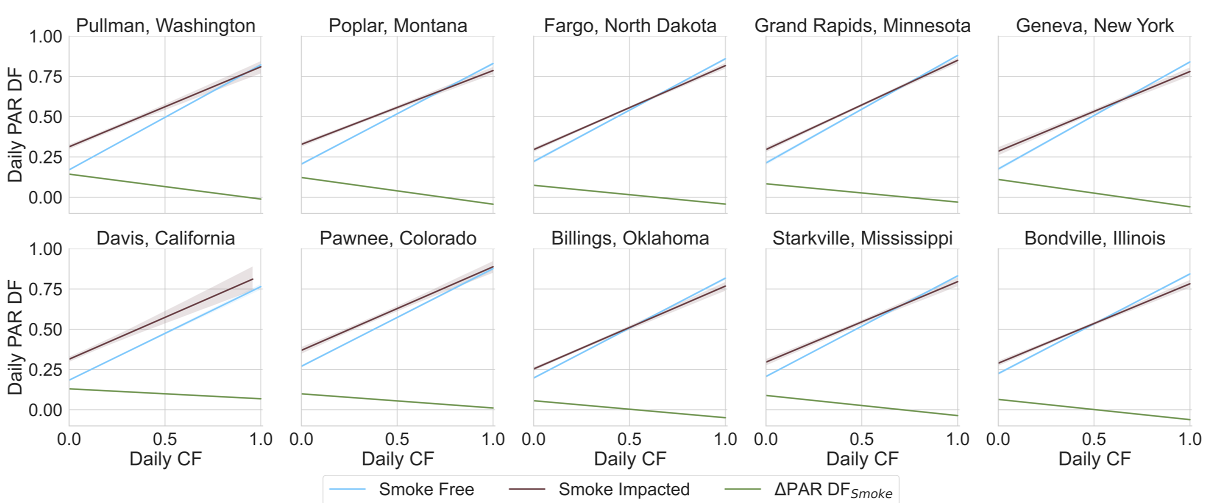

Figure 7: Linear regressions showing daily PAR DF by CF for all growing season days at each UVMRP site analyzed from 2006-2020 on smoke-impacted (brown) and smoke-free (blue) days. Shading of the same color indicates the 95% confidence intervals. The change in PAR DF (ΔPAR DF_{Smoke}) between smoke-impacted and smoke-free days is presented in green.

The site-specific analysis presented in Figure 7 indicates similar trends across all 10 sites—daily PAR DF increases on smoke-impacted days, particularly those with minimal to no clouds. On clear-sky days, the increase in PAR DF (ΔPAR DF_{Smoke}) with smoke ranges from 0.06 to 0.14. The greatest increase in PAR DF occurs at sites in the NW (0.14) and SW (0.13), which are closer to large wildfire ignitions. Sites further east and south in the GP, SP, MW, and SE exhibit smaller increases in PAR DF with smoke (0.06-0.08). Sites in the RM region experience increases in PAR DF from 0.10-0.12, while the NE site has a similar clear-sky increase in PAR DF of 0.11. Smoke-impacted days correspond to an increase in PAR DF across all cloud fractions at two sites: California and Colorado. At the other sites, PAR DF increases with smoke until high CF conditions are reached with this CF threshold ranging from 0.52 at the Illinois site to 0.93 at the Washington site. At all sites, the rate at which smoke increases PAR DF declines with increasing CF. Overall, smoke corresponds to higher PAR DF across more CF conditions at sites in the SW, NW, and RM regions, which are located closer to large western wildfires.

3.4 Impact of Smoke on Spectral Diffuse Fraction and Total Spectral Irradiance Under Cloud Free Conditions

Given that smoke-driven increases in PAR DF are greatest under clear-sky conditions, we present a more detailed spectral analysis of DF and total irradiance on clear-sky days (CF < 0.01) in Figures 8 and 9. Across the six MFRSR wavelengths measured between 368-870 nm, spectral DF is higher (Figure 8a) and total spectral irradiance is lower (Figure 8b) on smoke-impacted clear-sky days. The increase in spectral DF is greatest at 415 nm and 500 nm (+0.11) and least at 870 nm (+0.05). In the visible range, Mie scattering by smoke aerosols and absorption by brown carbon and NO_2 are more efficient at shorter wavelengths, preferentially increasing the diffuse component and decreasing total irradiance, respectively. As such, both processes work to increase DF at shorter wavelengths, which means that systems reliant on shorter wavelengths in the visible range will be more strongly impacted by smoke than those reliant on longer wavelengths. The reduction in total spectral irradiance is also greatest at 415 nm and 500 nm (-0.07 W/m^2) and least at the shortest (368 nm: -0.04 W/m^2) and longest wavelengths (870 nm: -0.02 W/m^2). Spectral DF increases on average by 45% (range: 20-62%) and total spectral irradiance decreases on average by 6% (range: 3-8%) with smoke.

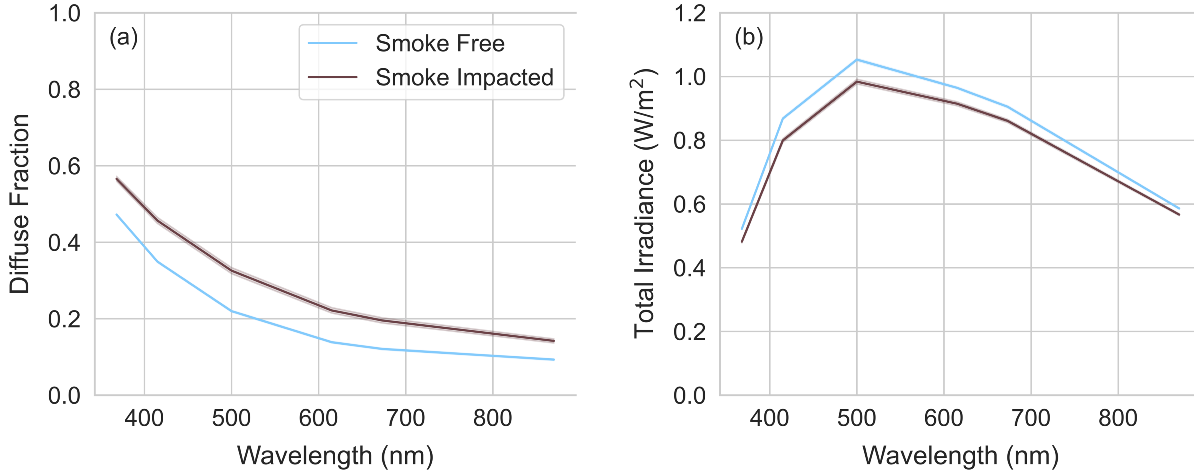

Figure 8: Variation in spectral diffuse fraction (a) and total spectral irradiance (b) at six MFRSR measured wavelengths on smoke-impacted (brown) and smoke-free (blue) clear-sky days during the growing season ($n_{smoke\text{-}free}$ = 2,562; $n_{smoke\text{-}impacted}$ = 1,003). Solid lines indicates the average value and shading shows the 95% confidence interval.

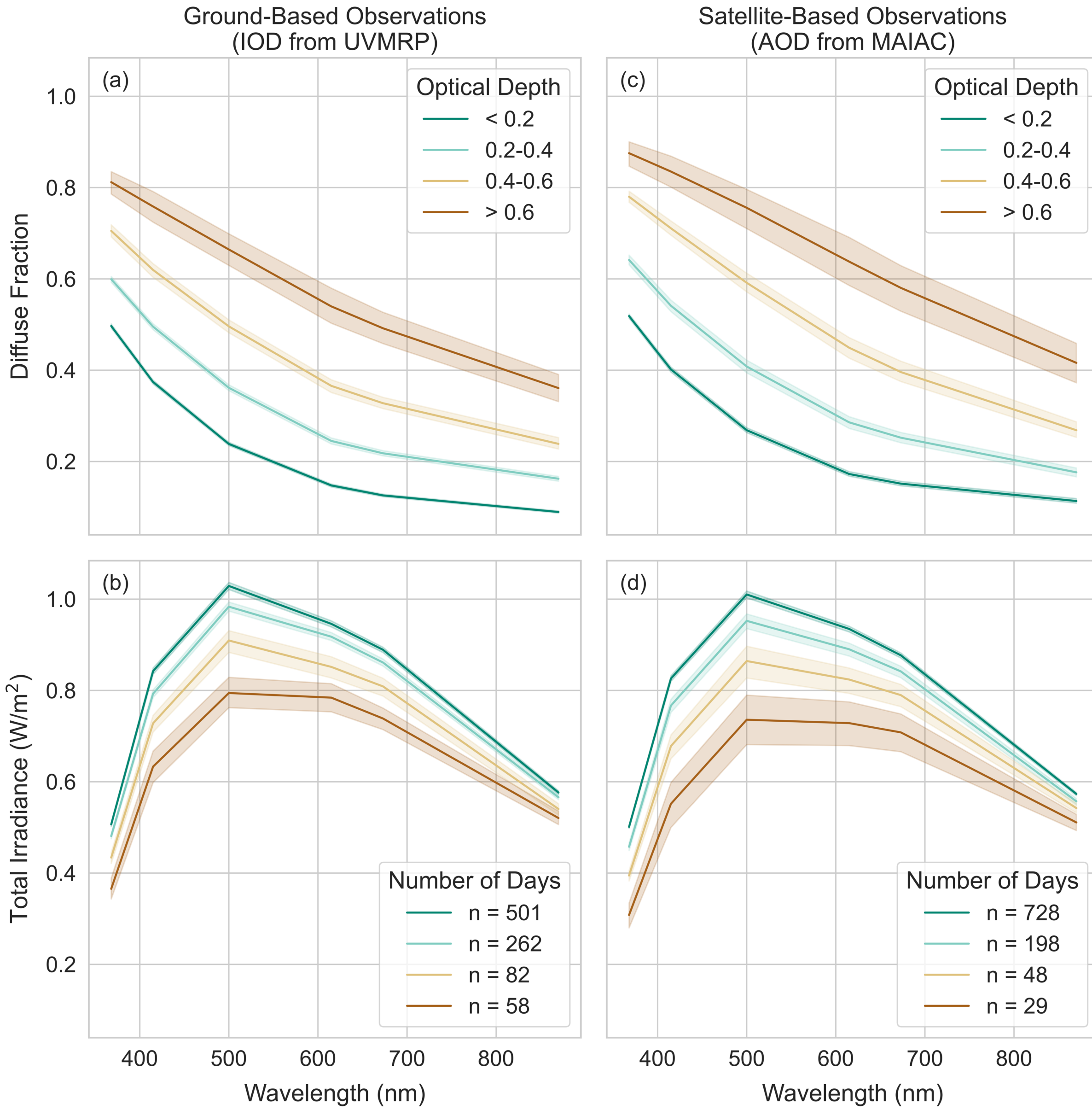

Figure 9: Variation in spectral diffuse fraction (a, c) and total spectral irradiance (b, d) across the six MFRSR wavelengths measured on smoke-impacted clear-sky days during the growing season. The impact of smoke plume thickness on irradiance measures is shown using different optical depths based on ground measurements of IOD from the UVMPR (a, b) and satellite retrievals of AOD by MAIAC (c, d). Solid lines indicates the average value and shading shows the 95% confidence interval (n_{uvmrp} = 903; n_{maiac} = 1003).

Isolating smoke-impacted clear-sky days, Figure 9 shows the impact of smoke plume thickness on DF and total irradiance at the spectral level. We use optical depth as a plume thickness proxy and compare results from the site-specific ground-based MFRSR measurements (Figure 9a/b) to those from satellite retrievals (Figure 9c/d). The former relies on optical depths calculated using Langley analysis and represents instantaneous cloud-aerosol optical depths

(IOD). The latter are aerosol optical depths (AOD) computed using the MAIAC algorithm to minimize smoke-cloud confusion and ensure AOD retrieval on smoke-impacted days.

The ground measurements show that DF (Figure 9a) becomes progressively larger as optical depth increases on smoke-impacted clear-sky days, which indicates a larger increase in DF under thick smoke plumes than under thin smoke plumes. Conversely, total irradiance (Figure 9b) decreases with increasing optical depth or plume thickness. Changes to total irradiance based on plume thickness are greatest at 500 nm, and least at 368 nm and 870 nm. Changes to DF, on the other hand, are relatively consistent across individual wavelengths. An optical depth increase from < 0.2 to 0.2-0.4 results in an increase in DF between 0.07 and 0.12 (average: +0.10) depending on the wavelength. A similar magnitude increase occurs when the optical depth increases to 0.4-0.6 (range: +0.08-0.13; average: +0.11) and again to > 0.6 (range: +0.11-0.17; average: +0.15). Days with thick smoke plumes (> 0.6; n = 58) occur less frequently than days with thin smoke plumes (< 0.2; n = 501), which results in wider 95% confidence intervals.

Ground-based sensors provide detailed information about radiation at specific sites; however, monitoring networks like the UVMRP are sparsely distributed. To expand beyond single sites and examine the impact of smoke on radiation at a national level requires satellite observations. Figure 9 compares DF and total irradiance trends from ground-based measures of plume thicknesses to measures from the MODIS satellite instrument. Using the MAIAC AOD (Figure 9c/d) as a plume thickness proxy results in similar spectral DF and total spectral irradiance trends to those found using the MFRSR IOD observations (Figure 9a/b). DF becomes progressively larger as the optical depth increases on clear-sky days, indicating that thick smoke plumes increase DF more substantially than thin plumes.

However, DF values for each wavelength and optical depth bin are slightly higher (range: +0.01-0.10; average: +0.05) when plume thickness is determined using MAIAC AOD rather than MFRSR IOD. The offset in DF values between the two methods is smaller when optical depths are lower (i.e., smoke plumes are thinner). Across the six wavelengths assessed, the average offset between the two methods for the optical depth bins < 0.2, 0.2-0.4, 0.4-0.6, and > 0.6 are +0.03, +0.04, +0.07, and +0.08, respectively. Total irradiances decrease with increasing optical depth for plume thicknesses regardless of which optical depth measure is used, but most irradiances are slightly lower when plume thicknesses are calculated with the MAIAC AOD. As with the DF comparison, the difference between the two methods is smaller when optical depths or plume thicknesses are lower. The average difference between the two methods for the optical depth bins < 0.2, 0.2-0.4, 0.4-0.6 are -0.01, -0.02, -0.03, and -0.05, respectively. Overall, Figure 9 highlights the similarity between DF and total irradiance trends derived using the MFRSR and MODIS instrument data, which supports the use of MAIAC AOD to examine smoke-driven radiation changes at larger scales.

4 Conclusions

We combine ground and satellite observations to examine spatial and temporal trends in smoke presence across the U.S. during the growing season as well as smoke's impact on diffuse fraction and total irradiance at the surface. The following conclusions stem from this analysis:

1. On average, smoke was present overhead on 20% of growing season days from 2006-2020 at the ten UVMRP sites analyzed. Over that 15 year period, interannual trends show an increase in smoke frequency.
2. Annual site-specific smoke frequency varies with the prevalence of wildfires in smoke source regions, but northern sites in the RM, GP, and MW regions consistently experience smoke the most often.
3. Monthly trends show that smoke frequency increases as the growing season progresses and peaks in August at sites in all regions, except the SE where the smoke source is distinctly different. The high frequency of smoke over most of the U.S. in July and August aligns with the mid- to late growing season when plants have larger leaf areas and more developed canopies that result in more shaded leaves. As such, smoke coincides with the period when plants benefit most from increases in PAR DF through the DRFE.
4. Using the UVMRP data, we show elevated daily PAR DF values occur on smoke-impacted days across a wide range of cloud conditions. There is an increase in the median and interquartile range of PAR DF on smoke-impacted days up to a CF of 0.5. Previous literature shows that increasing PAR DF to 0.45 is optimal for improving plant productivity (Knohl and Baldocchi, 2008). Our analysis shows that a PAR DF of 0.45 is achieved at a CF of 0.29 on smoke-impacted days, compared to a CF of 0.39 on smoke-free days. PAR DF increases most substantially on smoke-impacted days under cloud-free conditions (+0.10). On clear-sky days, the presence of smoke increases spectral DF and decreases total spectral irradiance at all six wavelengths measured by the MFRSR from 368-870 nm.
5. When smoke is present, spectral DF increases and total spectral irradiance decreases with increasing smoke plume thickness. Optical depth observations from ground (UVMRP) and satellite (MODIS MAIAC) instruments produce similar trends for the impact of plume thickness on DF and total irradiance.

Our analysis provides a foundation for further research on the impact of smoke on PAR and the use of the UVMRP network data. The observed interannual and seasonal variability in smoke exposure supports the use of UVMRP sites to characterize changes in PAR DF and total PAR associated with wildfire smoke and, in the future, to examine smoke-induced changes to agricultural crop yields within and across sites. Future work could focus on developing a model of PAR DF and total PAR on smoke-impacted days using data from all 34 UVMRP sites in the contiguous U.S. Expanding the number of stations included will allow us to better characterize smoke and irradiance variability within regions, especially in the Great Plains and Midwest where understanding smoke's impact on PAR is essential for understanding smoke's impact on agricultural production. The inclusion of satellite AOD measurements supports scaling this analysis to the regional and national level and may allow for additional atmospheric chemistry applications.

Acknowledgments

This material is based upon work supported by the National Science Foundation under Grant No. 1828902. We thank UVMRP program director Dr. Wei Gao, Becky Olson, and the rest of the

UVMRP staff (https://uvb.nrel.colostate.edu/UVB/) for maintaining the UVMRP instrument network and database as well as for assisting with data retrieval. Thank you to Drs. Jeffrey R. Pierce and J. Christine Chiu for advice on data products and subject matter expertise. We also thank Dr. Joshua Hewitt for statistical discussions.

Open Research

UVMRP data used in this analysis are publically available at https://uvb.nrel.colostate.edu/UVB. HMS data used in this analysis are publically available at https://www.ospo.noaa.gov/Products/land/hms.html. MAIAC data used in this analysis are publically available at https://modis-land.gsfc.nasa.gov/MAIAC.html. MODIS data used in this analysis are also publically available. The MOD08_D3 (Terra) product can be found at https://ladsweb.modaps.eosdis.nasa.gov/missions-and-measurements/products/MOD08_D3. The MYD08_D3 (Aqua) product can be found at https://ladsweb.modaps.eosdis.nasa.gov/missions-and-measurements/products/MYD08_D3. The final cleaned and merged dataset used in this analysis will be made available in Mountain Scholar upon publication along with all Python code files used to clean, merge, analyze, and visualize these data.

References

Abatzoglou, J. T., Battisti, D. S., Williams, A. P., Hansen, W. D., Harvey, B. J., & Kolden, C. A. (2021). Projected increases in western US forest fire despite growing fuel constraints. *Communications Earth & Environment 2021 2:1*, *2*(1), 1–8. https://doi.org/10.1038/s43247-021-00299-0

Abatzoglou, J. T., & Williams, A. P. (2016). Impact of anthropogenic climate change on wildfire across western US forests. *Proc. Natl Acad. Sci.*, *113*(42), 11770–11775. https://doi.org/10.1073/pnas.1607171113

Baker, K. R., Koplitz, S. N., Foley, K. M., Avey, L., & Hawkins, A. (2019). Characterizing grassland fire activity in the Flint Hills region and air quality using satellite and routine surface monitor data. *Science of The Total Environment*, *659*, 1555–1566. https://doi.org/10.1016/J.SCITOTENV.2018.12.427

Bigelow, D. S., Slusser, J. R., Beaubien, A. F., & Gibson, J. H. (1998). The USDA Ultraviolet Radiation Monitoring Program. *Bulletin of the American Meteorological Society*, *79*(4), 601–615. https://doi.org/10.1175/1520-0477(1998)079<0601:TUURMP>2.0.CO;2

Biggs, W. (1986). Radiation Measurement. In W. G. Gensler (Ed.), *Advanced Agricultural Instrumentation: Design and Use* (pp. 3–20). Springer Netherlands. https://doi.org/10.1007/978-94-009-4404-6_1

Brey, S. J., Ruminski, M., Atwood, S. A., & Fischer, E. v. (2018). Connecting smoke plumes to sources using Hazard Mapping System (HMS) smoke and fire location data over North America. *Atmospheric Chemistry and Physics*, *18*(3), 1745–1761. https://doi.org/10.5194/acp-18-1745-2018

Buchholz, R. R., Park, M., Worden, H. M., Tang, W., Edwards, D. P., Gaubert, B., Deeter, M. N., Sullivan, T., Ru, M., Chin, M., Levy, R. C., Zheng, B., & Magzamen, S. (2022). New seasonal pattern of pollution emerges from changing North American wildfires. *Nature Communications 2022 13:1*, *13*(1), 1–9. https://doi.org/10.1038/s41467-022-29623-8

Ford, B., Martin, M. V., Zelasky, S. E., Fischer, E. v, Anenberg, S. C., Heald, C. L., & Pierce, J. R. (2018). Future Fire Impacts on Smoke Concentrations, Visibility, and Health in the Contiguous United States. *GeoHealth*, *2*, 229–247. https://doi.org/10.1029/2018GH000144

Greenwald, R., Bergin, M. H., Xu, J., Cohan, D., Hoogenboom, G., & Chameides, W. L. (2006). The influence of aerosols on crop production: A study using the CERES crop model. *Agricultural Systems*, *89*(2–3), 390–413. https://doi.org/10.1016/j.agsy.2005.10.004

Hallar, A. G., Molotch, N. P., Hand, J. L., Livneh, B., McCubbin, I. B., Petersen, R., Michalsky, J., Lowenthal, D., & Kunkel, K. E. (2017). Impacts of increasing aridity and wildfires on aerosol loading in the intermountain Western US. *Environmental Research Letters*, *12*(1), 014006. https://doi.org/10.1088/1748-9326/AA510A

Harrison, L., Michalsky, J., & Berndt, J. (1994). Automated multifilter rotating shadow-band radiometer: an instrument for optical depth and radiation measurements. *Applied Optics*, *33*(22), 5118. https://doi.org/10.1364/ao.33.005118

Hemes, K. S., Verfaillie, J., & Baldocchi, D. D. (2020). Wildfire-Smoke Aerosols Lead to Increased Light Use Efficiency Among Agricultural and Restored Wetland Land Uses in

California's Central Valley. *Journal of Geophysical Research: Biogeosciences*, *125*(2), 1–21. https://doi.org/10.1029/2019JG005380

Higuera, P. E., & Abatzoglou, J. T. (2021). Record-setting climate enabled the extraordinary 2020 fire season in the western United States. *Global Change Biology*, *27*, 1–2. https://doi.org/10.1111/gcb.15388

Jethva, H., Torres, O., & Yoshida, Y. (2019). Accuracy assessment of MODIS land aerosol optical thickness algorithms using AERONET measurements over North America. *Atmospheric Measurement Techniques*, *12*, 4291–4307. https://doi.org/10.5194/AMT-12-4291-2019

Kanniah, K. D., Beringer, J., North, P., & Hutley, L. (2012). Control of atmospheric particles on diffuse radiation and terrestrial plant productivity: A review. *Progress in Physical Geography*, *36*(2), 209–237. https://doi.org/10.1177/0309133311434244

Knohl, A., & Baldocchi, D. D. (2008). Effects of diffuse radiation on canopy gas exchange processes in a forest ecosystem. *Journal of Geophysical Research: Biogeosciences*, *113*(2), 1–17. https://doi.org/10.1029/2007JG000663

Lee, S. C., Knox, S. H., McKendry, I., & Black, T. A. (2022). Biogeochemical and biophysical responses to episodes of wildfire smoke from natural ecosystems in southwestern British Columbia, Canada. *Atmospheric Chemistry and Physics*, *22*(4), 2333–2349. https://doi.org/10.5194/ACP-22-2333-2022

Lyapustin, A., & Wang, Y. (2018). *MODIS Multi-Angle Implementation of Atmospheric Correction (MAIAC) Data User's Guide Collection 6 (ver. of June 2018) Version 2.0*.

Lyapustin, A., Wang, Y., Korkin, S., & Huang, D. (2018). MODIS Collection 6 MAIAC algorithm. *Atmos. Meas. Tech*, *11*, 5741–5765. https://doi.org/10.5194/amt-11-5741-2018

McClure, C. D., & Jaffe, D. A. (2018). US particulate matter air quality improves except in wildfire-prone areas. *Proceedings of the National Academy of Sciences of the United States of America*, *115*(31), 7901–7906. https://doi.org/10.1073/pnas.1804353115

McKendry, I. G., Christen, A., Lee, S.-C., Ferrara, M., Strawbridge, K. B., O'Neill, N., & Black, A. (2019). Impacts of an intense wildfire smoke episode on surface radiation, energy and carbon fluxes in southwestern British Columbia, Canada. *Atmospheric Chemistry and Physics*, *19*(2), 835–846. https://doi.org/10.5194/acp-19-835-2019

Möhler, R. L., & Goodin, D. G. (2012). Mapping Burned Areas in the Flint Hills of Kansas and Oklahoma, 2000—2010. *Great Plains Research*, *22*, 15–25. https://about.jstor.org/terms

O'Dell, K., Bilsback, K., Ford, B., Martenies, S. E., Magzamen, S., Fischer, E. v., & Pierce, J. R. (2021). Estimated Mortality and Morbidity Attributable to Smoke Plumes in the United States: Not Just a Western US Problem. *GeoHealth*, *5*(9). https://doi.org/10.1029/2021GH000457

O'Dell, K., Ford, B., Fischer, E. v., & Pierce, J. R. (2019). Contribution of Wildland-Fire Smoke to US PM 2.5 and Its Influence on Recent Trends. *Environmental Science and Technology*, *53*, 1797–1804. https://doi.org/10.1021/acs.est.8b05430

Peppler, R. A., Bahrmann, C. P., Barnard, J. C., Campbell, J. R., Cheng, M. D., Ferrare, R. A., Halthore, R. N., Heilman, L. A., Hlavka, D. L., Laulainen, N. S., Lin, C. J., Ogren, J. A., Poellot, M. R., Remer, L. A., Sassen, K., Spinhirne, J. D., Splitt, M. E., & Turner, D. D. (2000). ARM Southern Great Plains Site Observations of the Smoke Pall Associated with the 1998 Central American Fires. *Bulletin of the American Meteorological Society*, *81*(11), 2563–2591. https://doi.org/10.1175/1520-0477(2000)081<2563:ASGPSO>2.3.CO;2

Platnick, S., & et al. (2015). MODIS Atmosphere L3 Daily Product. In *NASA MODIS Adaptive Processing System*. Goddard Space Flight Center. http://dx.doi.org/10.5067/MODIS/MOD08_D3.061

Rogers, C. M., & Bowman, K. P. (2001). Transport of smoke from the Central American fires of 1998. *Journal of Geophysical Research: Atmospheres*, *106*(D22), 28357–28368. https://doi.org/10.1029/2000JD000187

Rolph, G. D., Draxler, R. R., Stein, A. F., Taylor, A., Ruminski, M. G., Kondragunta, S., Zeng, J., Huang, H.-C., Manikin, G., McQueen, J. T., & Davidson, P. M. (2009). Description and Verification of the NOAA Smoke Forecasting System: The 2007 Fire Season. *Weather and Forecasting*, *24*(2), 361–378. https://doi.org/10.1175/2008WAF2222165.1

Ruminski, M., Kondragunta, S., Draxler, R., & Zeng, J. (2006). *Recent changes to the Hazard Mapping System*. 15th Int. Emiss. Inventory Conf. https://www.researchgate.net/publication/228625934_Recent_changes_to_the_Hazard_Mapping_System

Schiferl, L. D., & Heald, C. L. (2018). Particulate matter air pollution may offset ozone damage to global crop production. *Atmospheric Chemistry and Physics*, *18*(8), 5953–5966. https://doi.org/10.5194/acp-18-5953-2018

Val Martin, M., Heald, C. L., Lamarque, J. F., Tilmes, S., Emmons, L. K., & Schichtel, B. A. (2015). How emissions, climate, and land use change will impact mid-century air quality over the United States: A focus on effects at national parks. *Atmospheric Chemistry and Physics*, *15*(5), 2805–2823. https://doi.org/10.5194/ACP-15-2805-2015

Wang, J., van den Heever, S. C., & Reid, J. S. (2009). A conceptual model for the link between Central American biomass burning aerosols and severe weather over the south central United States. *Environmental Research Letters*, *4*(1), 015003. https://doi.org/10.1088/1748-9326/4/1/015003

Wang, S. C., Wang, Y., Estes, M., Lei, R., Talbot, R., Zhu, L., & Hou, P. (2018). Transport of Central American Fire Emissions to the U.S. Gulf Coast: Climatological Pathways and Impacts on Ozone and PM2.5. *Journal of Geophysical Research: Atmospheres*, *123*(15), 8344–8361. https://doi.org/10.1029/2018JD028684

Westerling, A. L. (2016). Increasing western US forest wildfire activity: sensitivity to changes in the timing of spring. *Philosophical Transactions of the Royal Society B*, *371*(20150178). https://doi.org/10.1098/rstb.2015.0178

Westerling, A. L., Gershunov, A., Brown, T. J., Cayan, D. R., & Dettinger, M. D. (2003). Climate and Wildfire in the Western United States. *Bulletin of the American Meteorological Society*, *84*(5), 595–604. https://doi.org/10.1175/BAMS-84-5-595

Westerling, A. L., Hidalgo, H. G., Cayan, D. R., & Swetnam, T. W. (2006). Warming and Earlier Spring Increase Western U.S. Forest Wildfire Activity. *Science*, *313*(5789), 940–943. https://doi.org/10.1126/SCIENCE.1128834

Xue, Z., Gupta, P., & Christopher, S. (2021). Satellite-based estimation of the impacts of summertime wildfires on PM 2.5 concentration in the United States. *Atmos. Chem. Phys*, *21*, 11243–11256. https://doi.org/10.5194/acp-21-11243-2021

Yue, X., Mickley, L. J., Logan, J. A., & Kaplan, J. O. (2013). Ensemble projections of wildfire activity and carbonaceous aerosol concentrations over the western United States in the mid-21st century. *Atmospheric Environment*, *77*, 767–780. https://doi.org/10.1016/J.ATMOSENV.2013.06.003